PAPER

Check for updates

Anodic SnO₂ porous nanostructures with rich grain boundaries for efficient CO₂ electroreduction to formate†

Ruizhen Ma,‡[b] Yan-Li Chen,‡[a] Yongli Shen,[b] Heng Wang,[b] Wei Zhang,*[a] Su-Seng Pang,[c] Jianfeng Huang,*[d] Yu Han [ID][e] and Yunfeng Zhao [ID] *[b]

Formic acid (HCOOH), the acidic form of formate, is an important hydrogen carrier which can be directly used in fuel cells. Development of earth-abundant element-based catalysts to convert carbon dioxide (CO_2) into HCOOH or formate with high selectivity and high efficiency has been a vigorous research activity in recent years but remains an unsolved challenge. In this contribution, using one-step anodization, we prepare nanotubular SnO_2 porous nanostructures with high surface area (90.1 m^2 g^{-1}), large porosity (0.74 cm^3 g^{-1}), and rich grain boundaries for electrochemical CO_2 reduction (CO_2RR). They exhibit stable 95% faradaic efficiency (FE) towards CO_2RR and 73% FE for formate at -0.8 V$_{RHE}$. The notable performance of such SnO_2 nanostructures can be attributed to their unique structural and chemical properties, which provide active sites for CO_2 adsorption and conversion, and easy access for CO_2 to the active sites. The insights gained from the structure/property relationships might be beneficial for designing superior electrocatalysts for CO_2 electroreduction into formate.

Introduction

Electrochemical CO_2 reduction (CO_2RR) to carbon-based fuels is a promising strategy for renewable energy storage and net carbon emission.[1–5] Liquid fuels, such as formic acid (HCOOH),[6–8] methanol[9] and ethanol,[10] produced *via* CO_2 electroreduction are actively sought because they can be directly used as energy-intensive carriers for fuel cells. Particularly, formic acid has been identified as an ideal hydrogen carrier owing to its high volumetric density (53.4 g H$_2$ L^{-1}), and low toxicity and volatility.[11] However, achieving highly efficient and selective electrocatalysts for converting

[a] State Key Laboratory of Quality Research in Chinese Medicine, Macau Institute for Applied Research in Medicine and Health, Macau University of Science and Technology, Taipa, Macau, China. E-mail: wzhang@must.edu.mo

[b] Tianjin Key Laboratory of Advanced Functional Porous Materials, Institute for New Energy Materials & Low-Carbon Technologies, School of Materials Science and Engineering, Tianjin University of Technology, Tianjin 300384, China. E-mail: yfzhao@tjut.edu.cn

[c] Faculty of Information, Macau University of Science and Technology, Taipa, Macau, China

[d] Multi-scale Porous Materials Center, Institute of Advanced Interdisciplinary Studies, School of Chemistry and Chemical Engineering, Chongqing University, Chongqing 400044, China. E-mail: jianfeng.huang@cqu.edu.cn

[e] Advanced Membranes and Porous Materials Center, King Abdullah University of Science and Technology, Thuwal 23955-6900, Kingdom of Saudi Arabia

† Electronic supplementary information (ESI) available. See DOI: 10.1039/d0ra03152f

‡ Ruizhen Ma and Yan-Li Chen contributed equally to this work.

CO_2 into HCOOH is challenging due to the myriad possible reaction pathways and sluggish reaction kinetics in the process of CO_2RR.

The formation of the intermediate $CO_2^{\cdot-}$ is a rate-determining step for CO_2RR in most pathways.[12] Metals like Pb, In, Zn, Sn, Pd and Bi, can hardly bind the intermediate $CO_2^{\cdot-}$ and hence are able to produce formic acid (or formate when pH > 3.8) at low overpotentials typically *via* the outer-sphere mechanism.[13] Among these metal-based electrocatalysts, Sn and its derivatives (*e.g.*, SnO_x, Sn alloy), as earth-abundant, low-cost and nontoxic materials, have attracted particular research interest, due to their capability of catalyzing CO_2 into formate with decent faradaic efficiencies (FEs) at moderate potentials.[14–21] For example, Meyer *et al.* found a maximum FE of 86% for formate at -1.8 V$_{SCE}$ when loading nanoscale SnO_2 particles on carbon black.[14] Xie *et al.* reported that Sn quantum sheets confined in graphene exhibited ∼89% FE towards formate at the same potential.[15] These results point out that the catalyst size and composition, which are correlated with the number and intrinsic properties of active sites exposed during CO_2 reduction, play important roles in determining the formation of formate. In addition, the electrocatalysis of CO_2 in aqueous solution is an electrochemical reaction at the three-phase interface of gas (CO_2), liquid (electrolyte) and solid (catalyst). The concentration of reactant CO_2 on the surface of the catalyst affects the electrocatalytic performance and is governed by at least two factors: (1) the CO_2 transport within the catalysts; (2) the CO_2 adsorption on

the catalysts. Therefore, the structure of the catalyst also matters critically in the formate formation activity. For example, hierarchical mesoporous SnO_2 nanosheets were reported to facilitate the mass transfer of CO_2, leading to a value of 87% FE for formate at a moderate overpotential (0.88 V).[16] SnO_2 nanowires with a high density of grain boundaries were proposed to enhance the CO_2 reduction into formate (ca. 80% FE at -0.8 V_{RHE}) via reforming the binding energy of the reactant or intermediates.[17] Taken together, these works conclude that formate production by CO_2RR is sensitive to a variety of parameters, including size, structure and composition etc. However, to date, it remains a challenge to incorporate these parameters to achieve an efficient electrocatalyst for the conversion of CO_2 to formate.

In this work, we report the results of an electrochemical study on the CO_2 reduction at SnO_2 porous nanostructures with integrated characteristics of high surface area, large porosity, and rich grain boundaries that favor the CO_2-to-formate conversion. The SnO_2 porous nanostructures were prepared by an anodization approach which is a facile yet effective technique for fabricating various porous metal oxides with ordered tubular nanostructure.[22] The as-prepared anodic SnO_2 porous nanostructures exhibit a tubular structure (pore-size: $\sim$45 nm) with abundant nanograins within the size range of 3–5 nm. The porous structure provides a large specific surface area (90.1 m^2 g^{-1}) and high porosity (0.74 cm^3 g^{-1}), while the grain boundaries render a strong CO_2 affinity with the heat of adsorption up to 50 kJ mol^{-1}, the upper limit of the physical adsorption. When tested as the electrocatalyst for the CO_2RR, the SnO_2 aerogels maintain 95% faradaic efficiency (FE) towards CO_2RR and 73% FE for HCOOH at -0.8 V vs. RHE for 12 h. Miscellaneous characterizations, including transmission electron microscope (TEM), N_2 (77 K) and CO_2 (273 and 298 K) adsorption, X-ray photoelectron spectroscopy (XPS) and electrochemistry, combined with theoretical calculations were employed to elucidate the correlations between the structure and composition of the aerogels and their CO_2RR performance.

Experimental section

Chemicals and instruments

Sn foil (thickness of 200 μm, purity > 99.99%, Renxin Metal), Nafion solution (5 wt%, Shanghai Hesen), Nafion® 117 cation exchange membrane (H⁺ form, Shanghai Hesen), carbon black (VULCAN XC72, Cabot), and other chemicals (Analytic Reagent) are used as received. The X-ray diffraction (XRD) was taken from Rigaku Ultima Iv. A scanning electron microscope (SEM, FEI, Verios 460L) and a high-resolution transmission electron microscope (HRTEM, FEI, Talos F200X) were utilized to characterize the morphology and high-resolution structure. X-ray photoelectron spectrometer (XPS) was determined on a Thermo Scientifica (ESCALAB250xi). Electrochemical measurements were carried on an electrochemical workstation (CHI760e, Shanghai CHI). Products in the gas phase were determined by a gas chromatograph (GC, 9790II, Zhejiang Fuli) equipped with thermal conductivity and a flame ionization

detector. Products in solution was detected by a nuclear magnetic resonance (NMR, Bruker, 400M).

Synthesis of SnO_2 tubular array by anodic oxidation

The surface oxide layer was firstly removed by soaking an Sn foil in a KOH solution (0.1 M) for 5 min, and then the Sn foil was ultrasonically cleaned in deionized (DI) water for later use. The anodization process was carried in a two-electrode cell, where the cleaned Sn foil was used as a working electrode and a graphite plate was used as the counter electrode with the distance of 1 cm. A constant voltage (8.0–12.0 V) was applied to the working electrode using a potentiostat instrument in a 0.5 M oxalic acid ($H_2C_2O_4 \cdot 2H_2O$, 99.5%) electrolyte for 5 min at room condition. After anodization, the Sn foil was repeatedly washed with DI water before ultrasonically stripped.

Fabrication of catalytic electrode

The electrode was fabricated through a dropping-coating method. Typically, SnO_2 powders (4 mg), carbon black (2 mg) and Nafion® solution (60 μL) were mixed with 1 mL mixture of DI water and ethanol (7 : 3 in v/v) and followed with ultrasonic treatment for 5 min to form a homogeneous ink. The suspension (80 μL) was dropped onto a glassy carbon electrode with an area of 1×1 cm^2 to form the catalyst layer with a loading amount of 300 μg cm^{-2} and the electrode were naturally dried for further electrochemical measurements.

Electrochemical measurement

All electrochemical CO_2 reductions were performed by using a well-sealed H-type cell with standard three-electrodes, in which two chambers were separated with a piece of Nafion® 117 membrane. One side of the H-cell was equipped with inlet and outlet, where CO_2 (99.99%) could be bubbled into the reaction cell through an inlet and the product in the gas phase would be introduced into a GC by the outlet. The area of the working electrode was 1 cm × 1 cm. An Ag/AgCl electrode (sat. KCl) was used as a reference electrode, and a Pt foil (99.999%, 1 cm × 1 cm) was used as a counter electrode, which was infiltrated into the electrolyte of 0.5 M $KHCO_3$ aqueous solution for all electrochemical testing. The cyclic voltammetry (CV) under potentials ranging from 0.4 to -1.0 V_{RHE} by varying the scan rate of 50 mV s^{-1}. The time–current curve was obtained by carrying out constant working potential at various potentials -0.7 to -1.2 V_{RHE}. Meanwhile, the average current density was obtained by dividing the total current by the geometric area of the working electrode. The potential values involved in this work were all calibrated to the potential of the reversible hydrogen electrode (RHE) by using eqn (1):[23]

$$E(vs.\ RHE) = E(vs.\ Ag/AgCl) + 0.197 + 0.0591 \times pH \qquad (1)$$

The high-purity CO_2 was continuously introduced into the electrolyte (0.5 M $KHCO_3$) for 30 min to make the solution reach a saturated state of CO_2 (pH = 7.2) before the electrochemical test. The flow rate of CO_2 gas was controlled to be 5 mL min^{-1} and the cathode chamber electrolyte was continuously stirred to accelerate

the bubble diffusion on the electrode surface at a rotation speed of 600 rpm during the electrolysis process. All tests for this work were controlled at room temperature and ambient pressure.

Product determination

The gas-phase products were quantified using a GC during 3 h long bulk electrolysis. Under the same test environment, the gas peak area detected by gas chromatography has a certain linear relationship with its actual concentration, so that the gas with known concentration can be used to calibrate and analyze the gas with unknown concentration, which combined with current density to calculate the faradaic efficiency (FE) by using eqn (2)–(4):[23]

$$j_{H_2} = ((\text{peak area})/\alpha) \times (\text{flow rate}) \times (2FP_0/RT) \\ \times (\text{electrode area})^{-1} \quad (2)$$

$$j_{CO} = ((\text{peak area})/\beta) \times (\text{flow rate}) \times (2FP_0/RT) \\ \times (\text{electrode area})^{-1} \quad (3)$$

$$FE_{H_2/CO} (\%) = (i_{H_2/CO}/i_{\text{total}}) \times 100 \\ = (V_{H_2/CO} \times Q \times (2FP_0/RT)) \times 100 \quad (4)$$

where, j_{H_2} and j_{CO} represent partial current densities of H_2 and CO, α and β represent peak area conversion coefficients of H_2 and CO calculated from standard GC mixtures, F is Faraday constant (96 485 C mol^{-1}), R is ideal gas constant (8.314 J (mol K)$^{-1}$), $P_0 = 1.013$ bar, $T = 273.15$ K.

The product in solution was detected and quantified by NMR. The 0.4 mL of post-cathodic reaction mixed with 0.1 mL deuteroxide (D_2O) and 0.1 mL dimethyl sulfoxide (DMSO, 100 ppm) as internal standard. The ^{1}H spectrum was measured with water suppression by a presaturation method. The area ratio of the formate peak to the DMSO peak was compared to the standard curve made by using sodium formate and the internal standard DMSO to calculate the amounts of formate products.

Computational details

All Spin-polarized calculations in this work are carried out using the Quickstep[24] module of the CP2K program package,[24,25]

a program developed for electronic structure calculations and molecular dynamics based on the Gaussian and plane waves formalism.[26] The generalized-gradient approximation (GGA) with spin-polarized revised PBE functional (revPBE) is selected to describe the exchange-correlation energy. All the structures and energies of the stationary points included in our work are evaluated at the DFT-D3 level with the approximation suggested by Grimme[27] added to the revPBE calculated energy. The wavefunctions were expanded in an optimized double-ζ Gaussian basis set[28,29] with a cutoff energy of 500 Rydberg.[30] Core electrons have been modeled by scalar relativistic norm-conserving pseudo potentials[30] with 4, 6, 1 and 4 valence electrons for Sn, O, H and C, respectively. Brillouin zone integration is performed with a reciprocal space mesh consisting of only the gamma point. The convergence criterion for the maximum force is set as 2×10^{-3}. Thermochemistry calculation is implemented by TAMkin,[31] a toolkit for normal mode analysis A (19.11 Å × 20.10 Å) and 5 O–Sn–O layers thick supercell has been selected to represent the $SnO_2\{110\}$ surface. A vacuum region between repeated slabs is set to be 30 Å, which ensures the negligible interaction between periodic replicas.

Results and discussion

Fig. 1 illustrates the typical fabrication of the porous SnO_2 nanostructures by the anodization approach wherein an Sn foil and a graphite plate were used as the anode and cathode, respectively, in an oxalic acid solution (0.5 M). After being applied with a specific voltage (i.e., 8, 10 and 12 V) for 5 min, the porous SnO_2 structures were formed on the surface of the Sn foil. They are hereafter denoted as SnO_2–AO_x (x: the anodization voltage). The SnO_2–AO_x layers can be easily exfoliated from the anode, and then used to construct the catalytic electrode for CO_2RR.

Fig. 2 and S1† report the structural characterization of the as-prepared SnO_2–AO_x aerogels by scanning electron microscopy (SEM) and transmission electron microscope (TEM). From the SEM of the SnO_2–AO_{10} (Fig. 2a and b), highly ordered porous structures are observed with the average pore size within the range of 40–50 nm (Fig. 2c). Varying the anodization voltage (i.e., 8 and 12 V) leads to similarly porous SnO_2–AO_8 and SnO_2–
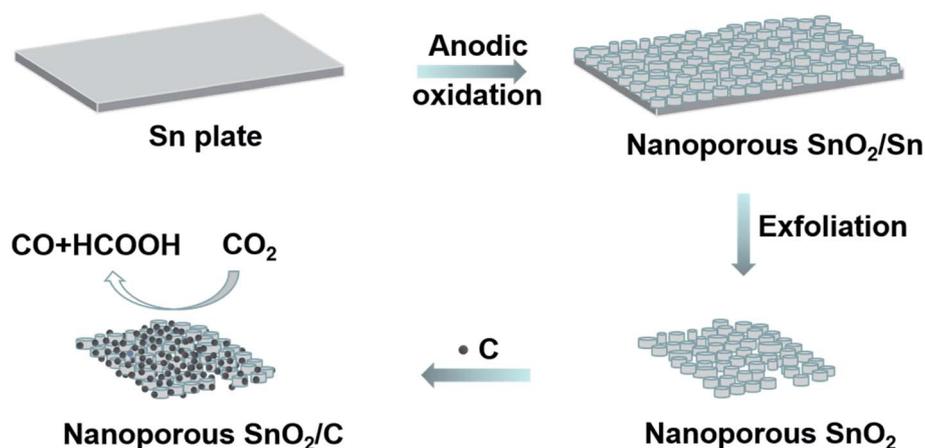

Fig. 1 Schematic representation of the fabrication of anodic SnO_2–AO_x porous nanostructures that are used as the electrocatalysts for CO_2RR.
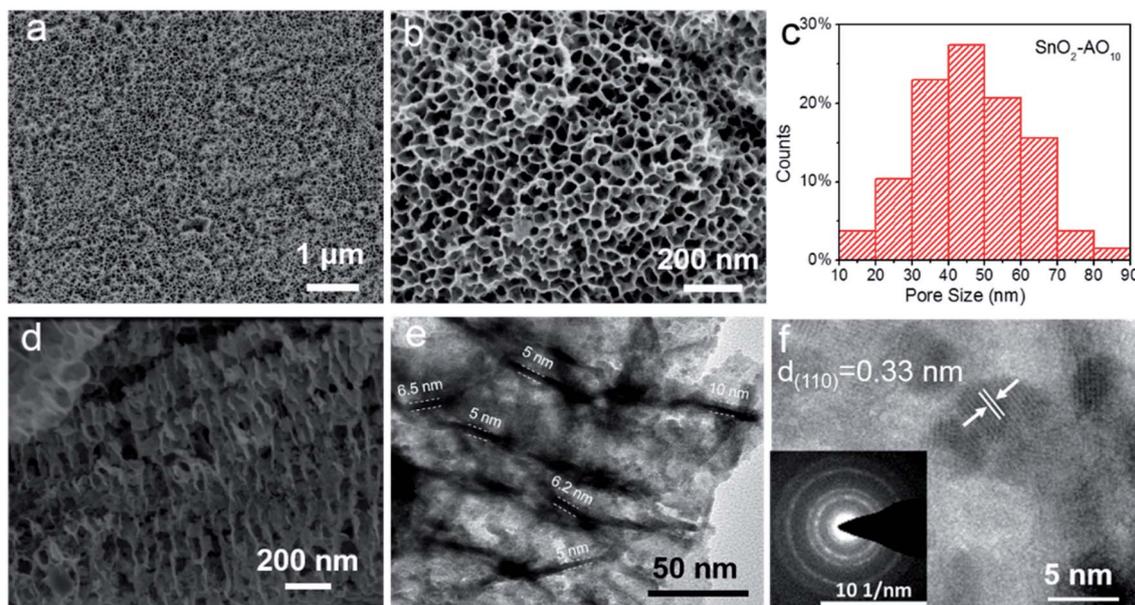
Fig. 2 (a and b) SEM images and (c) the corresponding pore size statistical analysis of the surface of SnO_2-AO_{10}. (d) SEM and (e) TEM images of the cross-section of SnO_2-AO_{10}. (f) High-resolution TEM image and the corresponding electron diffraction pattern (inset) of SnO_2-AO_{10}.

AO_{12} nanostructures with only slightly different pore sizes (Fig. S1†). The cross-section SEM image further illustrates that the porous SnO_2 layer is comprised of arrays of tubes that are nearly perpendicular to the Sn substrate (Fig. 2d and S2†). Here, the tubes are expected to promote the mass transfer and reaction during CO_2RR.[14] TEM was additionally employed to study the tubular structure, which shows that the wall thickness of the tubes is 5–10 nm (Fig. 2e). Interestingly, a closer view enabled by the high-resolution TEM (HRTEM) reveals that the tube walls are constituted by many small interconnected nanoparticles (3–

5 nm) through grain boundaries (Fig. 2f and S3†). The individual particles have good crystallinity, as indicated by the interplanar distance of 0.33 nm, which corresponds to the d-spacing of the (110) plane of SnO_2, and further confirmed by some discrete spots in the corresponding electron diffraction pattern of the HRTEM image (inset of Fig. 2f). In addition, the diffraction rings resulting from many spots very close together demonstrate the polycrystalline nature of the tube wall as a whole. Since ultra-small SnO_x nanoparticles and grain boundaries have been found to be active sites for CO_2RR,[16,17,32]
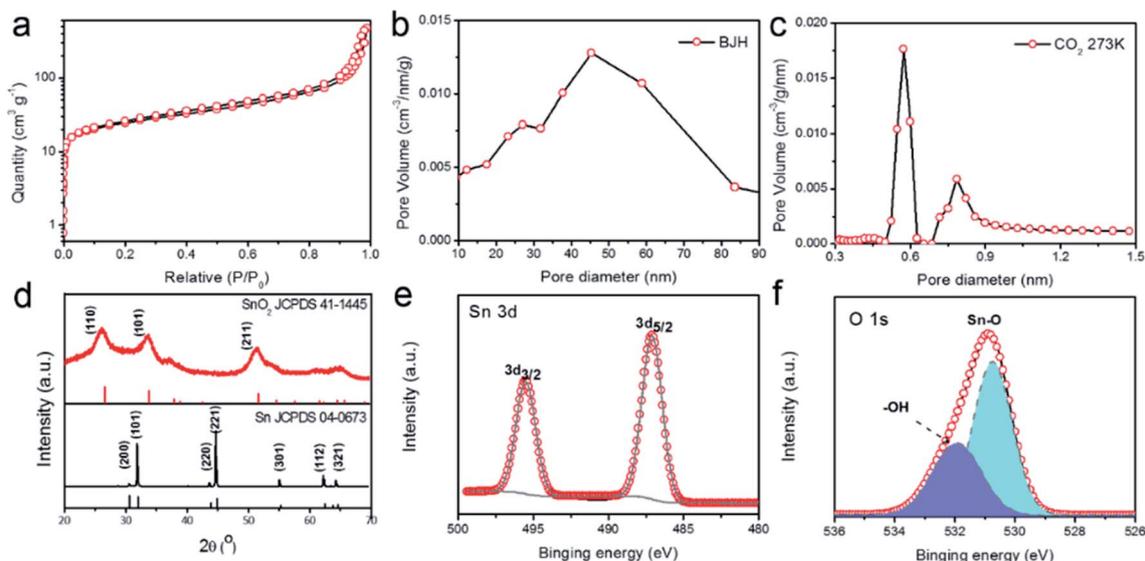

Fig. 3 (a) N_2 adsorption–desorption isotherm (at 77 K), (b) the corresponding pore size distribution calculated based on the desorption data of the isotherm, and (c) pore size distribution derived from CO_2 adsorption at 273 K, (d) XRD patterns of SnO_2-AO_{10} and Sn foil, (e) XPS Sn3d and (f) XPS O1s spectrum of SnO_2-AO_{10}.

the hierarchical SnO_2–AO_{10} nanostructures that feature tubular structure, ultra-small NPs and abundant grain boundaries show great promise for CO_2RR.

To gain more insights into the porous structure, N_2 adsorption–desorption isotherms at 77 K were measured to characterize the surface area and porosity of the SnO_2–AO_{10} nanostructures. As shown in Fig. 3a, the N_2 uptake increases slowly with the pressure in the low-pressure range then shoots up when P/P_0 exceeds 0.9. The isotherm thus belongs to the Type-II, as defined by IUPAC,[33] which indicates the presence of both micropores and mesopores in hierarchical porous structures. By applying the Barrett–Joyner–Halenda (BJH) method to the desorption data, the mesopores were found to be within an average size range of 40–50 nm (Fig. 3b), in good agreement with the SEM results (Fig. 2b and c) and reflecting the actual pores created by the anodic oxidation. On the basis of additional data of CO_2 adsorption at 273 K, the micropores were found to display a bimodal size distribution at 0.6 and 0.8 nm (Fig. 3c).

These micropores may arise from the gaps between nanoparticles in the tube walls, as revealed by the HRTEM image of the structure (Fig. 2f). Thanks to these pores of micro- and meso-sizes, the SnO_2–AO_{10} nanostructures exhibit an extremely high BET surface area (90.1 m^2 g^{-1}) and porosity (0.74 cm^3 g^{-1}). As a result, fast mass transport and easy access of reactants to the active sites during CO_2RR can be expected.

Finally, we investigated the crystal phase and chemical structure of the SnO_2–AO_{10} aerogels by X-ray diffraction (XRD, Fig. 3d) and X-ray photoelectron spectroscopy (XPS, Fig. 3e and f). From the XRD pattern, the diffraction peaks that can be

unambiguously indexed to rutile tetragonal SnO_2 (JCPDS card no. 41-1445) are observed, confirming the pure SnO_2 phase and crystallinity of SnO_2–AO_{10} nanostructures and demonstrating the successful conversion of pure Sn to SnO_2.[34] As a comparison, SnO_2–AO_8 and SnO_2–AO_{12} nanostructures exhibit similar pure SnO_2 phase but much poorer crystallinity (Fig. S4†). However, the mechanism as to how the anodization voltage affects the crystallinity is unclear at this moment, which will be examined in the future. Concerning the compositional information, the two peaks at 495.5 and 487.1 eV in the XPS spectrum are the characteristic peaks that can be assigned to Sn $3d_{3/2}$ and $3d_{5/2}$ ionizations, respectively, confirming the Sn^{4+} valence state of Sn element in the tin oxide aerogels (Fig. 3e).[34] Additionally, the XPS spectrum of O 1 s was collected (Fig. 3f). The peak fitting analysis verifies the oxygen bonding either with Sn as Sn–O bond (530.8 eV) or with H as –OH (531.9 eV) adsorbed on the aerogels surface.[35]

To evaluate the CO_2RR performance, we first examined the catalytic activity of SnO_2–AO_x nanostructures and an Sn plate by the Cyclic Voltammetry (CV) (Fig. 4a and S5†). In the N_2-saturated 0.5 M $KHCO_3$ solution, the marked increase in the cathodic current at ∼−0.80 V vs. RHE is associated with the hydrogen evolution reaction (HER), a parasite and competing reaction in aqueous solution against CO_2RR. By contrast, a more drastic current increase occurring at a much lower potential (−0.6 V_{RHE}) was observed in the CO_2-saturated 0.5 M $KHCO_3$ solution, meaning that the CO_2RR is catalytically more favored over HER on the SnO_2–AO_{10} catalysts. It is worth noting that the two cathodic peaks correspond to the reduction of SnO_2 to SnO (at −0.26 V_{RHE}) and SnO to Sn (at −0.34 V_{RHE}), while the anodic peaks arise from the oxidation of Sn to SnO (at −0.1 V)
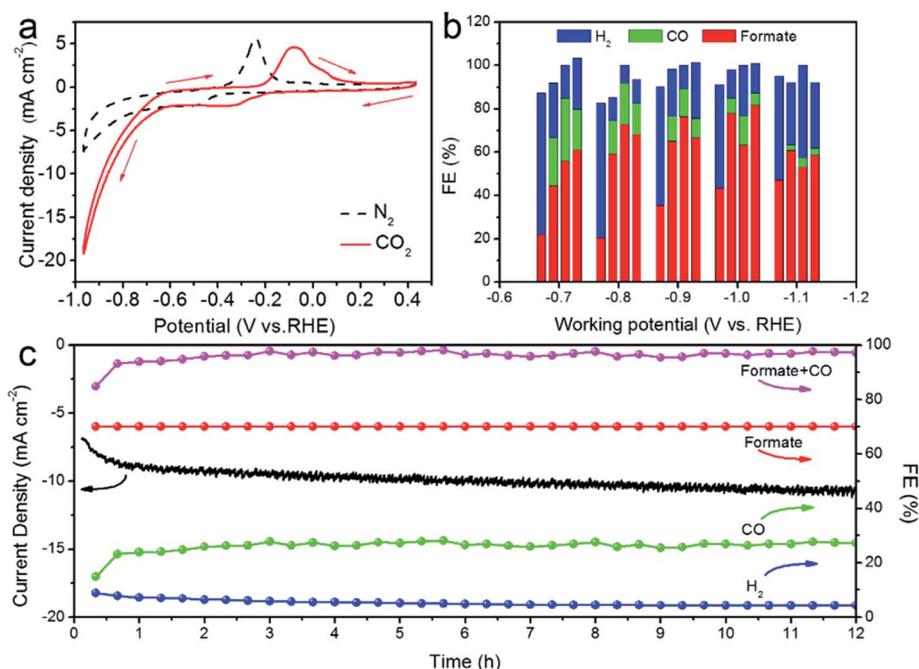

Fig. 4 (a) CV curves of SnO_2–AO_{10} in N_2- and CO_2-saturated 0.5 M $KHCO_3$ solution, scan rate: 50 mV s^{-1}. (b) FE of Sn plate, SnO_2–AO_8, SnO_2–AO_{10}, and SnO_2–AO_{12} (from left to right at each potential) for H_2, CO and formate. (c) Temporal evolution of the current density and FE toward H_2, CO, formate and CO + formate of the SnO_2–AO_{10} catalyst at −0.8 V_{RHE} for 12 h.

and SnO to SnO_2 (at 0.05 V).[34] As control samples, SnO_2–AO_8, SnO_2–AO_{12} and Sn electrode exhibit slightly more negative onset potentials ($\sim$−0.7 V_{RHE}) for the CO_2RR and much lower current density at each specific potential (Fig. S6,† for example, SnO_2–AO_8: $\sim$6 mA cm^{-2}, SnO_2–AO_{12}: $\sim$3 mA cm^{-2}, Sn: $\sim$2 mA cm^{-2}, SnO_2–AO_{10}: $\sim$10 mA cm^{-2} at −0.8 V_{RHE}). The lower activity of the other two SnO_2 nanostructures (*i.e.*, SnO_2–AO_8 and SnO_2–AO_{12}) might be due to their poorer crystallinity (Fig. S4†) which limits the electrical conductivity, as corroborated by the Electrochemical Impedance Spectroscopy (EIS) analysis of the electrodes made of the three SnO_2–AO_x nanostructures (Fig. S7†). Overall, the CV results demonstrate the superior CO_2RR activity of SnO_2–AO_{10} aerogels to those of the Sn plate and the SnO_2–AO_8 and SnO_2–AO_{12} nanostructures. We further assessed the selectivity (FE) of the SnO_2–AO_x nanostructures and Sn plate toward each product (*i.e.*, H_2, CO, formate) at potentials ranging from −0.7 to −1.1 V_{RHE}, the results of which are summarized in Fig. 4b and separately presented in Fig. S8–S12.† Consistent with previous reports,[12] the main products detected by NMR and GC during the electrolysis on the Sn plate are H_2 and formate (Fig. 4b, S8 and S9†). The FE for formate progressively increases with the potential from $\sim$20% at −0.7 V_{RHE} until reaching a maximum of $\sim$48% at −1.1 V_{RHE}. Conversely, H_2 dominates in the lower potential range (FE: $\sim$65% at −0.7 V_{RHE}).

Although the FE for H_2 drops as the potential becomes more negative, it sustains at a high level of $\sim$50% at −1.1 V_{RHE}, indicative of strong competition of HER against CO_2RR on the Sn plate. Interestingly, the anodization of the Sn plate resulted in a dramatic improvement in the CO_2RR. As illustrated in Fig. 4b and S10–S12,† utilizing SnO_2–AO_x nanostructures as the electrocatalyst generates an additional product, *i.e.* CO. The FE toward CO, which decreases with the increasingly negative potential, can be as high as $\sim$25% at low potentials of −0.7 and −0.8 V_{RHE}. Moreover, regardless of the potential, the formation of formate has been significantly boosted. For example, the highest FE achieved on SnO_2–AO_{12} ($\sim$82% at −1.0 V_{RHE}) corresponds to a $\sim$1.8-fold enhancement over that on the Sn plate ($\sim$46% at −1.0 V_{RHE}) and is even comparable with those state-of-the-art results ever reported (Table S1†). Concomitantly, HER is substantially suppressed. In particular, the FE for H_2 obtained over SnO_2–AO_{10} is critically below $\sim$5% at −0.8 V_{RHE}, in stark contrast with the $\sim$60% over the Sn plate. If we consider the total carbon conversion, the best performance is achieved over the SnO_2–AO_{10} aerogels which display $\sim$95% total FE (CO: $\sim$22%; formate: $\sim$73%) towards the CO_2RR at −0.8 V_{RHE}. Essentially, such a superior electrocatalytic performance can be well maintained, as evidenced by the stable current density and the C1 product (CO + formate) conversion, as well as the constantly low FE toward H_2 (<$\sim$5%) over a long-term electrolysis of 12 h (Fig. 4c). A plausible explanation for the high
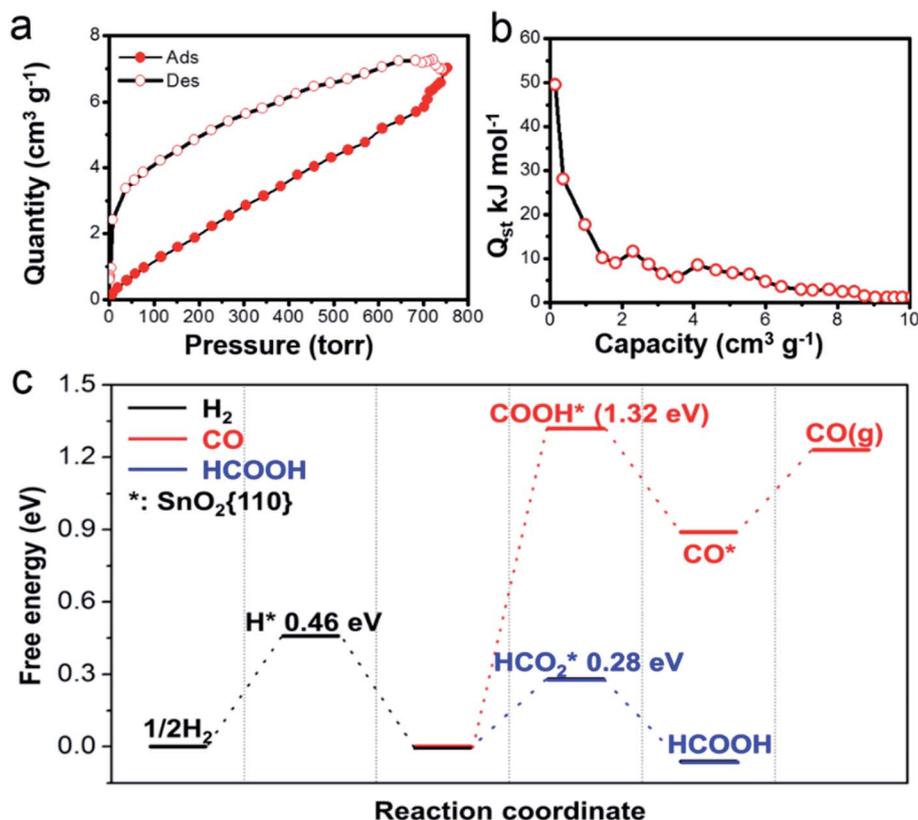

Fig. 5 (a) CO_2 adsorption–desorption isotherm at 298 K and (b) the corresponding heat of CO_2 adsorption derived from the isotherm by employing the Clausius–Clapeyron equation. (c) Free energy diagrams for the reaction pathways to H_2, CO and HCOOH on SnO_2 (110).

stability is good preservation of the porous structure, grain boundaries and the chemical state of the Sn species (*i.e.*, Sn^{4+}), as unravelled by the SEM, XRD and depth-dependent XPS characterizations on the post-mortem SnO_2–AO_{10} catalyst (Fig. S13–S15†). These structural and compositional parameters achieved by simply anodizing the Sn plate are thus the key to understanding the mechanism by which the anodic SnO_2 nanostructures promote pronouncedly the CO_2RR.

As suggested by earlier studies, porous structures are highly beneficial for CO_2RR because they provide a large surface area and facilitate the mass transfer.[36] Our SnO_2 aerogels should be particularly advantageous in this aspect, because of their unique porous structure. As a matter of fact, the BET surface area (90.1 $m^2\ g^{-1}$) for the SnO_2–AO_{10} nanostructures is considerably higher than that attained by most porous SnO_2 nanostructures (*e.g.*, SnO_2 porous nanowires: 35 $m^2\ g^{-1}$,[17] mesoporous tin oxide: 69.2 $m^2\ g^{-1}$,[36]) and reaches a comparable level to that of hierarchical mesoporous SnO_2 nanosheets (93.6 $m^2\ g^{-1}$).[16] Also, the EIS conducted on the SnO_2–AO_{10} electrode indeed shows a much-improved electrolyte (containing CO_2 in the form of $KHCO_3$) transfer over that on the Sn plate (Fig. S7†). In addition to the accessibility to the reactant, another important factor in determining the catalytic behavior is the intrinsic active sites the catalyst owns. As mentioned above, the SnO_2 aerogels present a high density of grain boundaries. Grain boundaries have been proposed to be enhanced active sites for CO_2RR due to their favorable electronic and chemical properties which tune the binding energy of the reaction intermediates.[37,38] Here, we further propose that the grain boundary might also benefit the CO_2 adsorption on the catalyst, the first step of CO_2RR. In an experiment of CO_2 adsorption–desorption on the SnO_2–AO_{10} nanostructures at 298 K (Fig. 5a), the isosteric heats of adsorption (Q_{st}) at zero coverage is found to be as high as 50 kJ mol^{-1} (Fig. 5b), which is the upper boundary of the CO_2 physical adsorption heat (25–50 kJ mol^{-1}) and approaches the chemical adsorption heat (60–90 kJ mol^{-1}).[39,40] Lastly, the chemical state of the Sn species should be also relevant, especially with the production of formate. Tin oxide has displayed remarkable activity and selectivity towards formate.[41,42] The Sn^{4+} species that can mostly survive (~85%, Fig. S14†) during CO_2RR are thus believed to play a crucial role in the formation of formate on SnO_2–AO_{10} aerogels. Advancing one step, we performed first-principles calculations to assess the key energy pathways of the formation of H_2, CO and formate on the SnO_2 (110) surface (see details in the ESI†). The free energy diagram in Fig. 5c clearly shows that the production of formic acid is energetically more favorable than either the evolution of H_2 or the formation of CO, thus confirming the importance of the tin oxide in driving the FE toward formate.

Conclusions

In summary, we have fabricated tubular SnO_2 nanostructures *via* facile anodization of an Sn plate. When tested as electrocatalysts for CO_2RR, the SnO_2 nanostructures can achieve a relatively high current density at moderate potentials for selective and stable production of formate. The outstanding performance can be attributed to a combination of factors related to the structural and compositional properties: (1) the high specific surface area (90.1 $m^2\ g^{-1}$) and large porosity (0.74 $cm^3\ g^{-1}$) enable easy access for CO_2 to the catalytic sites by amply exposing the active sites and advancing the electrolyte transfer; (2) the grain boundaries offer active sites for enhancing the CO_2 adsorption and tuning the binding energies of intermediates; (3) the Sn^{4+} species together with its good preservation under CO_2 conditions intrinsically dictates the selectivity for formate and inhibits the H_2 evolution. We expect this study to provide useful guidelines for developing porous electrocatalysts for efficient CO_2 electroreduction.

Conflicts of interest

There are no conflicts to declare.

Acknowledgements

Notes and references

1 D. D. Zhu, J. L. Liu and S. Z. Qiao, *Adv. Mater.*, 2016, **28**, 3423–3452.

2 J. F. Huang and R. Buonsanti, *Chem. Mater.*, 2019, **31**, 13–25.

3 F. J. Yu, P. H. Wei, Y. Yang, Y. H. Chen, L. M. Guo and Z. Q. Peng, *Nano Mater. Sci.*, 2019, **1**, 60–69.

4 J. F. Huang, N. Hörmann, E. Oveisi, A. Loiudice, G. L. De-Gregorio, O. Andreussi, N. Marzari and R. Buonsanti, *Nat. Commun.*, 2019, **9**, 3117.

5 Y. K. Chen, K. J. Chen, J. W. Fu, A. Yamaguchi, H. M. Li, H. Pan, J. H. Hu, M. Miyauchi and M. Liu, *Nano Mater. Sci.*, 2020, DOI: 10.1016/j.nanoms.2019.10.006.

6 R. Kortlever, I. Peters, S. Koper and M. T. M. Koper, *ACS Catal.*, 2015, **5**, 3916–3923.

7 T. N. Huan, P. Simon, G. Rousse, I. Genois, V. Artero and M. Fontecave, *Chem. Sci.*, 2017, **8**, 742–747.

8 S. B. Liu, J. Xiao, X. F. Lu, J. Wang, X. Wang and X. W. Lou, *Angew. Chem., Int. Ed.*, 2019, **58**, 8499–8503.

9 W.-H. Wang, Y. Himeda, J. T. Muckerman, G. F. Manbeck and E. Fujita, *Chem. Rev.*, 2015, **115**, 12936–12973.

10 Y. C. Li, Z. Wang, T. Yuan, D.-H. Nam, M. Luo, J. Wicks, B. Chen, J. Li, F. Li, F. P. G. de Arguer, Y. Wang, C.-T. Dinh, O. Voznyy, D. Sinton and E. H. Sargent, *J. Am. Chem. Soc.*, 2019, **141**, 8584–8591.

11 T. He, P. Pachfule, H. Wu, Q. Xu and P. Chen, *Nature Rev. Mater.*, 2016, **1**, 16059.

12 J.-P. Jones, G. K. S. Prakash and G. A. Olah, *Israel J. Chem.*, 2014, **54**, 1451–1466.

13 Y. Zheng, A. Vasileff, X. Zhou, Y. Jiao, M. Jaroniec and S.-Z. Qiao, *J. Am. Chem. Soc.*, 2019, **141**, 7646–7659.

14 S. Zhang, P. Kang and T. J. Meyer, *J. Am. Chem. Soc.*, 2014, **136**(5), 1734–1737.

15 F. C. Lei, W. Liu, Y. F. Sun, J. Q. Xu, K. T. Liu, L. Liang, T. Yao, B. C. Pan, S. Q. Wei and Y. Xie, *Nat. Commun.*, 2016, **7**, 12697.

16 F. Li, L. Chen, G. P. Knowles, D. R. MacFarlane and J. Zhang, *Angew. Chem., Int. Ed.*, 2017, **56**, 505–509.

17 B. Kumar, V. Atla, J. P. Brian, S. Kumari, T. Q. Nguyen, M. Sunkara and J. M. Spurgeon, *Angew. Chem., Int. Ed.*, 2017, **56**, 3645–3649.

18 S. Liu, F. Pang, Q. Zhang, R. Guo, Z. Wang, Y. Wang, W. Zhang and J. Ou, *Appl. Mater. Today*, 2018, **13**, 135–143.

19 X. Wang, J. Lv, J. X. Zhang, X. L. Wang, C. Z. Xue, G. Q. Bian, D. S. Li, Y. Wang and T. Wu, *Nanoscale*, 2020, **12**, 772–784.

20 Y.-W. Choi, F. Scholten, I. Sinev and B. R. Cuenya, *J. Am. Chem. Soc.*, 2019, **141**, 5261–5266.

21 J. Wang, Y. Ji, Q. Shao, R. Yin, J. Guo, Y. Li and X. Huang, *Nano Energy*, 2019, **59**, 138–145.

22 H. C. Shin, J. Dong and M. Liu, *Adv. Mater.*, 2004, **16**, 237–240.

23 K. Jiang, Y. F. Huang, G. S. Zeng, F. M. Toma, W. A. Goddard III and A. T. Bell, *ACS Energy Lett*, 2020, **5**, 1206–1214.

24 J. Vandevondele, M. Krack, F. Mohamed, M. Parrinello, T. Chassaing and J. Hutter, *Comput. Phys. Commun.*, 2005, **167**, 103–128.

25 CP2K version 4.1, CP2K is freely available from, http://www.cp2k.org.

26 B. Geraldlippert and J. Huttermicheleparrinello, *Mol. Phys.*, 1997, **92**, 477–488.

27 S. Grimme, J. Antony, S. Ehrlich and H. Krieg, *J. Chem. Phys.*, 2010, **132**, 154104–154119.

28 M. Fronzi, S. Piccinin, B. Delley, E. Traversa and C. Stampfl, *Phys. Chem. Chem. Phys.*, 2009, **11**, 9188–9199.

29 V. Shapovalov and H. Metiu, *J. Catal.*, 2007, **245**, 205–214.

30 S. Goedecker, M. Teter and J. Hutter, *Phys. Rev. B*, 1995, **54**, 1703–1710.

31 A. Ghysels, T. Verstraelen, K. Hemelsoet, M. Waroquier and S. V. Van, *J. Chem. Inf. Model.*, 2010, **50**, 1736–1750.

32 J. Gu, F. Heroguel, J. Luterbacher and X. Hu, *Angew. Chem., Int. Ed.*, 2018, **57**, 2943–2947.

33 M. Thommes, K. Kaneko, A. V. Neimark, J. P. Olivier, F. Rodriguez-Reinoso, J. Rouquerol and K. S. W. Sing, *Pure Appl. Chem.*, 2015, **87**, 1051–1069.

34 R. Daiyan, X. Lu, W. H. Saputera, Y. H. Ng and R. Amal, *ACS Sustainable Chem. Eng.*, 2018, **6**, 1670–1679.

35 L. Fan, X. Li, B. Yan, J. Feng, D. Xiong, D. Li, L. Gu, Y. Wen, S. Lawes and X. Sun, *Adv. Energy Mater.*, 2016, **6**, 1502057.

36 H. Ge, Z. Gu, P. Han, H. Shen, A. M. Al-Enizi, L. Zhang and G. Zheng, *J. Colloid Interface Sci.*, 2018, **531**, 564–569.

37 C. W. Li, J. Ciston and M. W. Kanan, *Nature*, 2014, **508**, 504.

38 K.-S. Kim, W. J. Kim, H.-K. Lim, E. K. Lee and H. Kim, *ACS Catal.*, 2016, **6**, 4443–4448.

39 Y.-S. Bae and R. Q. Snurr, *Angew. Chem., Int. Ed.*, 2011, **50**, 11586–11596.

40 T. Watabe and K. Yogo, *Sep. Purif. Technol.*, 2013, **120**, 20–23.

41 Y. Chen and M. W. Kanan, *J. Am. Chem. Soc.*, 2012, **134**, 1986–1989.

42 Q. Li, J. Fu, W. Zhu, Z. Chen, B. Shen, L. Wu, Z. Xi, T. Wang, G. Lu, J.-j. Zhu and S. Sun, *J. Am. Chem. Soc.*, 2017, **139**, 4290–4293.